Carbon 218 (2024) 118760

Contents lists available at ScienceDirect

Carbon

journal homepage: www.elsevier.com/locate/carbon

Carbon nano-onions: Individualization and enhanced water dispersibility

Matteo Andrea Lucherelli [a,**], Lisa M.S. Stiegler [b,c], Florian Steiger [d], E. Harriet Åhlgren [f,g], Julia Requena-Ramírez [a], Edison Castro [h,i], Luis Echegoyen [h,j], Andreas Hirsch [d,e], Wolfgang Peukert [b,c], Jani Kotakoski [f], Johannes Walter [b,c], M. Eugenia Pérez-Ojeda [d,***], Gonzalo Abellán [a,*]

[a] Instituto de Ciencia Molecular (ICMol), Universidad de Valencia, Calle Catedrático José Beltrán, 2, 46980, Paterna, Valencia, Spain
[b] Institute of Particle Technology (LFG), Friedrich-Alexander-Universität Erlangen-Nürnberg (FAU), Cauerstrasse 4, 91058, Erlangen, Germany
[c] Interdisciplinary Center for Functional Particle Systems (FPS), Friedrich-Alexander-Universität Erlangen-Nürnberg (FAU), Haberstrasse 9a, 91058, Erlangen, Germany
[d] Department of Chemistry and Pharmacy, Friedrich-Alexander University of Erlangen-Nuremberg, Chair of Organic Chemistry II, Nikolaus-Fiebiger-Str. 10, 91058, Erlangen, Germany
[e] Joint Institute of Advanced Materials and Processes (ZMP), Friedrich-Alexander University of Erlangen-Nuremberg, Dr.-Mack-Str. 81, D-90762, Fürth, Germany
[f] Faculty of Physics, University of Vienna, Boltzmanngasse 5, 1090, Vienna, Austria
[g] Department of Physics, University of Helsinki, P.O. Box 43, 00014, Helsinki, Finland
[h] Department of Chemistry, University of Texas at El Paso, El Paso, TX, 79968, USA
[i] PTC Therapeutics, Inc., 350 North Bernardo Avenue Mountain View, CA, 94043, USA
[j] Institute of Chemical Research of Catalonia (ICIQ), Av. Països Catalans, 16, Tarragona, E-43007, Spain

ARTICLE INFO

Keywords:
Carbon nano-onions
Carbon materials
Analytical ultracentrifugation
Materials chemistry
Exfoliation

ABSTRACT

Carbon nano-onions (CNOs) are a unique class of carbon nanomaterials, with a concentric fullerene-like structure and sp^2-hybridized carbon atoms. Onions present high mechanical strength, good conductivity, the capability to intercalate alkali metals, showing promising applications in diverse fields, such as tribology, energy storage, and nanomedicine. Their production has been developed by several techniques, with the most interesting being the thermal annealing of carbon nanodiamonds because of the easy scalability (gram-scale) and morphologic control (size and shape form perfectly spherical to polygonal). However, this synthesis is commonly affected by the formation of strong aggregates larger than 100 nm, attributed to carbon soot formation or strong van der Waals interactions, hindering the work with small and individual particles, leading to an altered yield of functionalization. In this study we propose a method for CNO individualization based on strong acid treatment, yielding highly water dispersible nanoparticles. Analytical ultracentrifugation (AUC) analysis is employed as a technique to investigate the particle dimensions directly in dispersion, permitting an ensemble analysis free from further sample preparation bias. Moreover, we also provide a comprehensive evaluation of the common post-synthetic treatment methods, and their effects. By means of scanning transmission electron microscopy with medium angle annular dark field detector and electron energy loss spectroscopy (STEM-MAADF and EELS) we have shown images of individual CNOs. Their successful separation achieved in this study is significant for future research and applications in nanomedicine, electrochemistry, and materials composites, where sample homogeneity is critical.

1. Introduction

Carbon nanomaterials are a large family constituted of morphologically different carbon allotropes, with two- (2D), mono- (1D) and zero- (0D) dimensional materials [1]. Graphene and carbon nanotubes, with their characteristic 2D and 1D morphologies respectively, are the two most famous members of the family. These, together with fullerenes and carbon dots (OD), have been widely investigated, while carbon nano-onions (CNOs) represent a less explored, but very interesting and promising 0D form.

* Corresponding author.
** Corresponding author.
*** Corresponding author.
E-mail addresses: matteo.lucherelli@uv.es (M.A. Lucherelli), eugenia.perez-ojeda@fau.de (M.E. Pérez-Ojeda), gonzalo.abellan@uv.es (G. Abellán).

https://doi.org/10.1016/j.carbon.2023.118760
Received 16 October 2023; Received in revised form 17 December 2023; Accepted 21 December 2023
Available online 22 December 2023

CNOs are carbon allotropes characterized by a crystalline structure consisting of a series of concentric shells of graphitic carbon, with an interlayer distance of ca. 0.344 nm. They were first reported by Ugarte in 1992, obtained by *in-situ* strong irradiation of carbon soot at 300 kV in a high-resolution transmission electron microscope [2]. From their matryoshka-like structure arose several interesting properties, such as high mechanical resistance, conductivity [3], intercalation of alkali metals [4], and surface chemical functionalization that maintain their main properties [5]. This makes CNO suitable materials for different fields, such as tribology [6], supercapacitors [7,8], energy storage [9] and also for biomedical applications [10].

One of the great advantages of CNOs compared to the other carbon allotropes is their production methods, allowing the gram-scale synthesis of the material with controlled dimension from 2 to more than 50 nm [3]. Since their first observation, several methods have been developed, mainly starting from carbon nanodiamonds (ND), based on water arc discharge [11,12], ND detonation [13], mechanical milling [14], or thermal annealing [15–17], to mention a few [3]. Thermal annealing represents the easiest method for scalable industrial production, which is also capable of producing controllable and reproducible particles. The synthesis can be modified by varying the precursor size production conditions and the maximum annealing temperature (T_{max}), in this way tuning the CNOs morphology. ND sp^3-to-sp^2 conversion begins above 600 °C, with the formation of amorphous carbon structures, that evolve in outer graphitic crystalline layers by carbon lattice rearrangement at temperatures ranging between 900 and 1100 °C [18,19]. The transformation occurs from the outside to the inside of the particles, leading to the complete ND conversion at T_{max}>1500 °C. Below this temperature, the coexistence of hybrid crystalline-amorphous particles is observed, including the presence of unreacted ND cores. When T_{max}>1900 °C, the carbon lattice evolves, mainly forming polyhedral structures, leading to samples with lower morphological homogeneity [20]. Of fundamental interest are CNOs physical states after synthesis. As reported by Presser and co-workers, the reaction atmosphere plays an important role in the final particle's aggregation [21]. CNOs produced under vacuum appear to be more separated and less defective compared to onions produced in argon atmosphere, with aggregates larger than 100 nm, while also containing nanographene particles [17,20,21]. Aggregates were observed by dynamic light scattering (DLS) and reported for CNOs produced from ND detonation [22], as well as for CNOs produced under argon [17,20,21] or helium atmosphere, and after reductive-route covalent functionalization [4].

Until now, this behavior has been attributed to two main reasons: I) strong van der Waals and π–π stacking interactions, diminishing the CNOs' solvent dispersibility and increasing aggregation [23,24]; II) the presence of an amorphous carbon soot or a small graphitic layer, aggregating the onions and hindering their separation [22]. The first one could be easily addressed by the employ of suitable solvents, whose chemical-physical properties have been calculated to be the most appropriated for their stabilization (e.g. N-Methyl-2-pyrrolidone (NMP)), as in the case of 2D materials [25,26]. The second case would require approaches capable of amorphous carbon removal. Following this direction, post-production annealing treatment at 525 °C of CNOs was reported to be sufficient to reduce or remove the amorphous carbon layers, increasing the inter-onions gas permeability [21]. After similar treatment at 400 °C, our group reported the alkali metal intercalation of the CNOs' outer layers, demonstrating the importance of the onions surface defects [4]. However, in all the previously mentioned cases, a hydrodynamic radius larger than 100 nm was always reported, with a size distribution depending on the production conditions [27–29]. To the best of our knowledge, only one example, where CNOs produced by underwater arc discharge and further functionalized with BODIPY moieties, reported DLS experiments with a size distributions of ~5 nm [30]. It is clear that, despite the interest around CNO synthesis and purification methods, there is still a lack of information about their aggregation state, especially when dispersed in solution. Different studies demonstrated CNO dispersibility using surfactants, chemical functionalization and surface oxidation, as well as biodegradability, however without addressing the material's size distribution [24,31–35]. Regardless, achieving water dispersibility for individualized CNOs remains an open challenge.

Along this front, the hypothesis behind our investigation is that CNO aggregates can be ascribed not only to amorphous carbon soot, but also to the formation of covalent connections between onions and fused particles [36,37], generated during its formation, similarly to what was reported for C_{60} fullerene network formation or to polymers vulcanization processes [38]. This could also explain the relatively low functionalization degree observed for CNOs. In fact, the formation of a covalent network would limit the access of the reagents to the onions external layer, allowing for functionalization primarily on the external surface of the aggregates [4,16].

The aim of this work is to develop a chemical method to obtain individualized CNOs, leading to dispersions free from aggregation, while also identifying the most appropriate characterization techniques (Scheme 1).

Herein, we will demonstrate the harsh acid treatment led to individual CNOs (Scheme 1). In contrast, mild treatments do not show efficacy for CNOs individualization but maintain large aggregates, albeit better dispersible in solvents. The particles distribution in solution will be proven by application of analytical ultracentrifugation (AUC) analysis. Thanks to the *real-time* combination of centrifugation and absorption measurement, in dependence of time and the radial position of the measuring cell, this technique permits to determine the entire bulk particle distribution. Finally, HRTEM and STEM-MAADF EELS images of individual CNOs undoubtedly support our findings on individualization. The advances in CNO treatment demonstrated in this work will play a fundamental role in the future development of research in fields such as nanomedicine, electrochemistry, and composite materials, where sample homogeneity is of paramount importance.

2. Materials and methods

CNOs were obtained by thermal annealing of carbon nanodiamonds in He atmosphere at a temperature of 1650 °C and further annealed at 400 °C (1 h, under air) as previously described [4]. Horn tip sonication was performed using a SONICS, ultrasonic processor GEX750 instrument. Centrifugation was performed using an Eppendorf centrifuge 5810R. All reagents employed were from Sigma-Aldrich. The samples employed in the study were produced as following:

1) p-CNOs: A dispersion of pristine CNOs was obtained in N-methyl-2-pyrrolidone (NMP, 1 mg/mL) by 1 h horn sonication (20% amplitude, 1s sonication, 1s pause) maintaining the temperature lower than 30 °C using an ice bath.
2) p-CNOs-15h sample — Mechanical treatment: p-CNOs were sonicated by a horn sonicator for 15 h at 40% amplitude with a 2s sonication + 1s pause program (NMP 1 mg/mL). The temperature was maintained below 30 °C using an ice bath.
3) 6M-CNOs and ox-CNOs: CNOs dispersions (3 mg/mL, 20–30 mL) in nitric acid (6 M or concentrated (~15.8 M)) were obtained by 30 min bath sonication. The dispersions were heated at 120 °C for 48 h in a round bottom flask equipped with a reflux system. In the first case, ~60% of the initial material mass was recovered, while for concentrated acid solutions the recovered material was between 20 and 30% depending on the batch.
4) NH_4OH–CNOs: A CNO dispersion (3 mg/mL, 20–30 mL) in 1:1 H_2O_2/NH_4OH (concentrated solutions) was obtained by bath sonication (30 min). The mixture was stirred at 80 °C for one day in a round bottom flask equipped with a reflux system. After the treatment, ~90% of the initial material was recovered after purification.

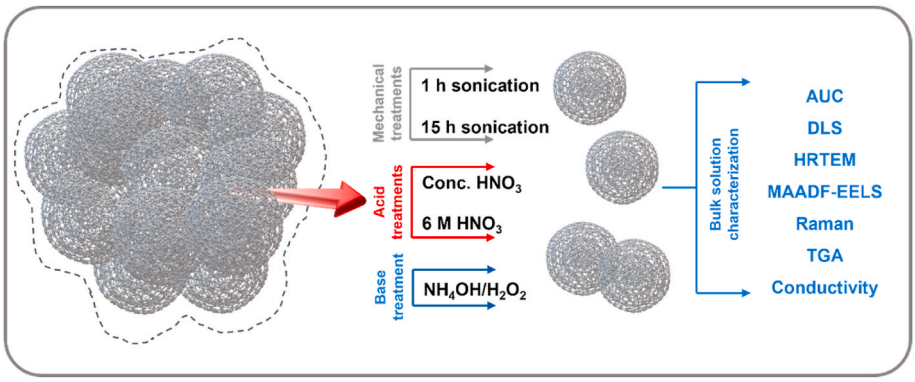

Scheme 1. Schematic representation of the CNOs separation treatments and their characterization.

Work-up was performed by a first centrifugation step at 18500 RCF (xg) for 30 min at 5 °C. The precipitate was washed twice by centrifugation in a H_2O/*i*-propanol 4:6 mixture, then twice in an *i*-propanol-hexane 1:1 mixture to finish with a hexane solution. Finally, the recovered pellet was dried under vacuum overnight.

Analytical Ultracentrifugation (AUC): Analytical Ultracentrifugation experiments were conducted with a user-modified preparative Optima L-90K ultracentrifuge from Beckman Coulter equipped with a multiwavelength extinction detector from Nanolytics Instruments. Further details about the method and the device can be found in previous works [39,40]. For sample preparation, the CNO dispersions in either NMP or water were diluted so that the extinction of each sample ended up at or below unity at a wavelength of 425 nm (Lambert-Beer region). For the measurement, 400 μL of each dispersion was filled into a measuring cell equipped with a two-sector titanium centerpiece with an optical path length of 12 mm from Nanolytics Instruments. Sedimentation velocity measurements were carried out at a rotor speed of 15000 rpm while the temperature was kept constant at 20 °C. All data were evaluated at a wavelength of 425 nm with the SEDFIT software (version 16.1c) using the ls-g*(s) method to receive the apparent sedimentation coefficient distribution of each sample with a resolution of 150 grid points. The data analysis included regularization by the second derivative for which a confidence level (F-ratio) of 0.95 was chosen. The meniscus position was fit for each sample and radial and time-invariant noise were also corrected during data analysis.

Raman spectroscopy: Statistical Raman mapping was performed with a LabRAM Aramis (Horiba) confocal Raman microscope equipped with an automated XYZ table (Märzhäuser) and a laser spot size of approximately 1 μm (100× objective, NA = 0.90). All measurements were conducted using an excitation wavelength of 532 nm, D2 filter (incident laser energy approximately 0.21 mW), and acquisition times of 5 s and 2 accumulations with a grating of 1800 g/mm. Raman mappings were recorded on a 19 μm by 19 μm map, giving 361 single-point spectra that were averaged for all samples. The spectrometer was calibrated to the frequency of diamond (1332 cm^{-1}). Spectra analysis was performed with Labspec software (Horiba) equally for all measurements. All data points of Raman mappings were baseline corrected using a polygonal correction, despiked and the baseline noise was shifted to zero. Raman peak analysis and fitting was performed using 8 different Lorentzian peaks. The raw data of D, G and 2D bands of all individual and average spectra was extracted and plotted using OriginPro (OriginLab). All displayed values are derived from the fittings of the individual spectra.

High-resolution transmission electron microscopy (HRTEM): HRTEM images were recorded with a 200 kV field emission transmission electron microscope (FEG) with a resolution (Point Resolution) of 0.24 nm. The instrument is equipped with a CCD GATAN camera and "Digital Micrograph", software for image acquisition and treatment.

STEM and EELS: Scanning transmission electron microscopy (STEM) and electron energy loss spectroscopy (EELS) analyses were carried out with the aberration corrected dedicated STEM instrument Nion UltraSTEM 100. The highest pressure in the system is in the range of 10^{-8} mbar, the typical pressure inside the sample area of the microscope is 10^{-9} mbar. The microscope was operated at 60 kV, and the images were recorded with the medium angle annular dark field (MAADF) detector with an annular range of 60–200 mrad and with the high angle annular dark field (HAADF) detector with the annular range of 80–300 mrad. The convergence semiangle of the electron probe is 30 mrad. The EELS acquisition setup consists of a Gatan PEELS 666 spectrometer retrofitted with an Andor iXon 897 electron-multiplying charge-coupled device (EMCCD) camera. The individual spectra were background subtracted by fitting power law to the spectrum before the oxygen K edge (with an onset at 532 eV). Furthermore, in additional cases, the individual spectra were scaled by the corresponding HAADF intensity to account for the varying thickness of the sample.

X-ray photoelectron spectroscopy (XPS): X-ray Photoelectron Spectroscopy (XPS) was performed on a Thermo Scientific K alpha X-ray photoelectron spectrometer, using a type of radiation: monochromatized Al K-alpha radiation (1486.6 eV) at $4*10^{-9}$ mBar. The samples were deposited on copper tape and the analysis was conducted using a laser spot of 400 μm.

Thermogravimetric analysis (TGA): Thermogravimetric analysis was carried out with the TGA 8000 Thermogravimetric analyzer (PerkinElmer) over a temperature range from 50 °C to 900 °C and a N_2 gas flow of 100 mL/min. The samples were first held at 50 °C for 15 min to ensure an inert atmosphere and consequently heated to 100 °C at 10 °C/min and held there for 2 min to ensure the removal of residual solvent. Lastly, samples were heated from 100 °C to 1000 °C at 10 °C/min.

Dynamic light scattering (DLS): The Zetasizer Nano series ZEN3600 (Malvern Instruments) was used for DLS and ζ-potential determination. The Zetasizer is equipped with a 633 nm He–Ne laser. All DLS measurements were performed at 25 °C, with an equilibration time of 60 s at an angle of 173° (NIBS, "noninvasive backscatter"). DTS0012 polystyrene cuvettes (water dispersions) and quartz cuvettes (NMP dispersions) were used to conduct measurements at 0.05 mg/mL sample concentration in water. Aqueous HCl and NaOH solutions were used to achieve the respective pH values. Three consecutive measurements were performed for each sample (50 scans per measurement) and averaged. Titration experiments were performed with the Zetasizer Nano series ZEN3600 and the MPT-2 Autotitrator (Malvern Instruments) using DTS1070 disposable folded capillary cells. The samples were titrated starting from pH 13 to pH 3 utilizing aqueous HCl and NaOH solutions (0.1 mol/L). Hydrodynamic diameters and ζ-potentials were measured every 0.5 pH value (±0.2 pH) three times.

Conductivity measurements: 5 mg of the CNOs powder was compressed to form a pellet, further cut to 1 × 2 $mm^{2,}$ and attached to the top of a printed circuit board. The material was connected to the board by platinum wires and conductive silver paint. The circuit board was connected to a Keithley 6517B electrometer, to measure I/V curves.

3. Results and discussion

3.1. CNOs treatment

The cleaning and individualization of CNO was investigated by screening different chemical methodologies previously employed for CNTs and CNOs [17,41,42]. Pristine CNOs were produced by thermal annealing at 1650 °C of carbon nanodiamonds under He atmosphere, as previously reported in other studies [43]. Their treatment was followed by a thermal annealing at 400 °C in atmospheric air, giving p-CNOs, employed as reference materials. This treatment was reported by several studies as an effective way to remove the excess of amorphous carbon and reduce the onions aggregation and was therefore applied as pre-treatment for samples homogenization. Chemical and physical treatments were applied to p-CNOs to increase their dispersibility and to separate/break the aggregates. Chemical separation was investigated dispersing p-CNOs in organic solvents and in acid or basic solutions, followed by heating or strong sonication as described in the following: I) p-CNOs sonicated by tip sonication for 1 h in NMP at 20 % amplitude were employed as reference material; II) 6 M and concentrated nitric acid (giving 6M-CNOs and ox-CNOs, respectively), 48 h at 120 °C; III) Base piranha mixture (1:1H_2O_2/NH_4OH concentrated solution) (NH_4OH–CNOs) [42]; IV) Lastly, to break aggregation by physical method, pristine CNOs were sonicated in NMP at high intensity (40 % amplitude) for 15 h (p-CNOs-15h).

Prior to any type of material characterization, it was evident at first glance that macroscopic changes in CNO dispersibility occurred after these treatments. Acid-treated CNOs presented high water dispersibility, and their sedimentation was not possible applying short centrifugation times (<30 min), once redispersed in MilliQ water. These dispersions required to be diluted in a 6:4 *i*-propanol/H_2O mixture. The particles sedimentation was then obtained by centrifugation at 18500 RCF at 5 °C (30 min centrifugation). On the other hand, NH_4OH–CNOs were easy to sediment with centrifugation at 1800 RCF in every solvent employed (NMP, water, or *i*-propanol). Moreover, both 6M − and ox-CNOs were easily redispersed in water by simple bath sonication after being dried, giving stable suspensions with little sedimentation for more than six months. Remarkably, ox-CNOs showed an absence of dispersibility in nonpolar solvents such as hexane, while p-CNOs and NH_4OH–CNOs presented poor water dispersibility, sedimenting shortly after dispersion by horn sonication. As expected, acid treatment increased the water dispersibility of CNOs, while base piranha treatment maintained the characteristic hydrophobicity of carbon materials.

3.2. Sedimentation analysis by analytical ultracentrifugation

AUC was used to study the disperse properties of differently treated CNOs in their desired solvent, which is NMP for p-CNOs, p-CNOs-15 h, and NH_4OH–CNOs or deionized water (DIW) for 6M − and ox-CNOs [23]. During sedimentation in an AUC experiment, the absorption at a sample-specific wavelength is tracked by a UV–Vis detector, and from the thereby obtained radial- and time-dependent sedimentation profiles, the sedimentation coefficient distribution can be obtained with excellent resolution and statistical significance by numerical modeling [44]. For our experiments, we chose a wavelength of 425 nm for data analysis, which is a good compromise of lamp signal and sample turbidity. The measurements were performed at a rotor speed of 15000 rpm, which was optimized after essaying lower speeds (3000, 5000, 10000 rpm) to be sufficient to induce sedimentation of smaller CNO fractions, while still being capable of tracking sedimentation of larger CNO fractions, giving thus a full overview of the sedimentation coefficient distribution for the whole sample. From the differential sedimentation coefficient distributions, the extinction-weighted cumulative sedimentation coefficient distributions were calculated. From this, we chose the median S_{50} value (in Sved) and deduced from it the median D_{50} value (in nm) based on formula (1). While the density and viscosity of the solvents are standard tabulated values, we assumed a density of 1.9 g/cm^3 for CNOs produced from ND thermal annealing at 1700 °C [9].

$$D_{50} = \left(\frac{18\eta_s S_{50}}{\rho_p - \rho_s}\right)^{1/2} \quad (1)$$

The span $\Phi = (D_{75} - D_{25})/D_{50}$ gives an indication of the broadness of the distribution and thus the polydispersity of the sample. Furthermore, the equivalent molar mass M_{50} (in kDa) was determined from D_{50}, when assuming that the CNOs employed were mostly constituted by particles with perfect spherical shape (further corroborated by microscopy characterization, section 3.3) [45,46]. General considerations on the dispersion behavior can be obtained from the differential sedimentation coefficient distributions (Fig. 1a). p-CNOs show a broad sedimentation coefficient distribution, while just a minor shift to lower Sved is observed for p-CNOs-15 h and NH_4OH–CNOs, suggesting that these treatments have minor capacity in the aggregates' reduction. On the other hand, the opposite is observed in the case of acid treatments. 6M-CNOs and ox-CNOs (in DIW), which exhibited a major shift to lower Sved with increasing nitric acid concentration corresponding to an increase in the particles separation. The same trend emerged when considering the cumulative sedimentation coefficient distributions and their related S_{50}, D_{50} values, and equivalent molar masses M_{50} (Fig. 1b and Table 1). Particle aggregation is most pronounced for p-CNOs, with a very broad size distribution and an average equivalent size of ~139 nm, representing a first confirmation of CNOs aggregation after thermal annealing production [21]. Base piranha treatment was reported to remove amorphous carbon from CNTs [42]. We applied this treatment to investigate whether the CNOs aggregation is dependent on the presence of an amorphous carbon soot. AUC analysis clearly showed a slight reduction of aggregation compared to p-CNOs (D_{50} ~ 92 nm) suggesting that aggregation is not dependent on amorphous carbon constraints. To prove whether the aggregation is dependent on strong van der Waals interactions, we prepared a dispersion applying strong tip sonication for prolonged time (15 h) in the most appropriate solvent (NMP). These conditions should be sufficient to promote separation, similarly to what was reported for other carbon materials exfoliation, like CNTs, graphene and other 2D materials [25,47,48]. However, even in this case, p-CNOs-15h distribution exhibited little deviation from p-CNOs (~107 nm). Because of its similarity with p-CNOs, p-CNOs-15h was discarded from the further characterization. Finally, concentrated nitric acid treatment was confirmed as the most effective approach for CNOs individualization. ox-CNOs show a narrowed distribution centered around two main populations with dimensions of ~6 and 9 nm (19.9 and 41.5 Sved, respectively) (Table S1), similar to what was previously evaluated by microscopic measurements for this material [8]. Nonetheless, despite the strong acidic treatment, aggregates with bigger size remain present, causing an increase of the median size to ~32 nm, the smallest obtained among the samples in this study and corresponding to small aggregates of 5–6 onions each. Hereby it is shown that the individualization of the CNOs leads to decreasing average sizes. However, the spans increase due to the presence of small amount of big agglomerates in the dispersion, even after oxidative treatment. Finally, treatment with 6 M nitric acid proved to be less effective in onion separation, with an average distribution of ~55 nm and the presence of a small prominent population with a D_{50} value of ~13 nm (12.9 Sved). A similar trend is also demonstrated when calculating the corresponding equivalent molar masses M_{50}, with values decreasing from 1612 MDa of p-CNOs aggregates to 18.9 MDa for ox-CNOs.

Supporting our hypothesis, the results retrieved from AUC analysis suggest that CNO aggregation is more strongly related to the covalent network than to particles constrained by a physical barrier. Indeed, in this latter case, long sonication or amorphous carbon removal treatment would be sufficient to overcome carbon soot containment or van der Waals interactions, leading to smaller, separated particles. These results are fundamental to making a distinction between dispersibility and

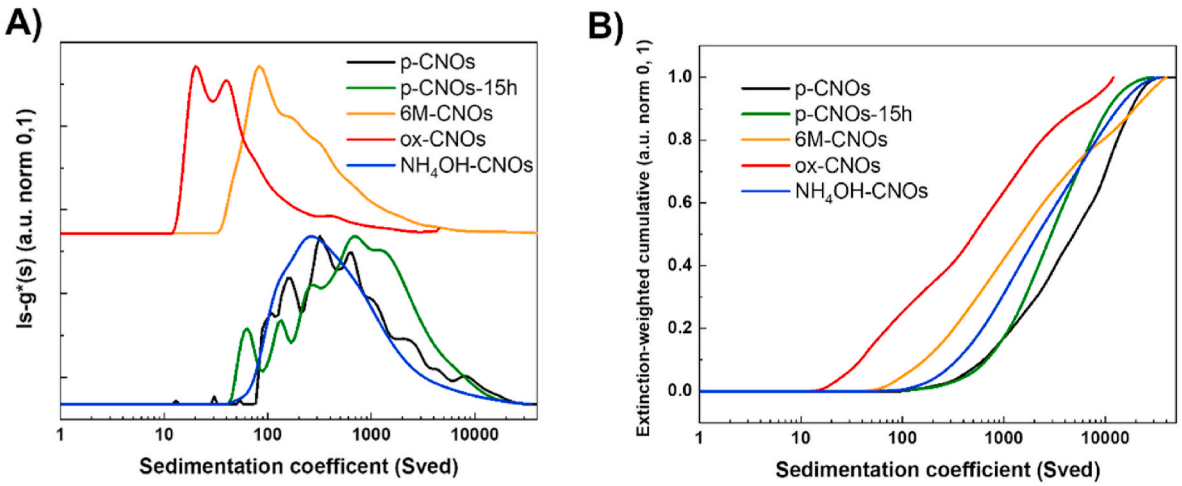

Fig. 1. A) Differential and (B) cumulative sedimentation coefficient distributions of dispersed CNO samples. For better comparability, the distributions were normalized to a value of 1 and were logarithmically plotted. (A colour version of this figure can be viewed online.)

Table 1
From the cumulative sedimentation coefficient distributions determined S_{50} values with thereof calculated D_{50} values, spans Φ and eq. molar masses M_{50}.

Sample	Solvent	S_{50} (Sved)	D_{50} (nm)	span Φ (a.u.)	Eq. Molar Mass M_{50} (MDa)	Centrifugation time (h)
p-CNOs	NMP	5182.94	139	0.91	1612	1.3
p-CNOs-15h	NMP	3077.88	107	0.76	738	1.2
NH_4OH–CNOs	NMP	2262.58	92	0.99	465	1.7
6M-CNOs	DIW	1526.64	55	1.44	101	1.8
ox-CNOs	DIW	501.10	32	1.45	19	4.9

separation of CNOs. As a matter of fact, appropriate solvents, and conventional treatments (3 or 6 M nitric acid, piranha base, sonication) lead to improved CNOs dispersibility due to surface oxo-functionalization (*vide infra*), nonetheless without a remarkable aggregate reduction. In turn, individualized ox-CNOs exhibit an enhanced water dispersibility requiring 5 h of ultracentrifugation (1814 RCF) to achieve complete sedimentation (Table 1).

Furthermore, for the sake of reproducibility, we extended our study to two more distinct CNOs batches, prepared under the same nominal conditions. These batches, namely p_2-CNOs and p_3-CNOs were subjected to concentrated nitric acid treatment, yielding ox_2-CNOs and ox_3-CNOs. In both cases, we observed similar behavior as for batch 1 (p-CNOs/ox-CNOs). After oxidation, a clear decrease in the S_{50}, D_{50} and M_{50}-values was observed compared to the pristine CNOs (Fig. S1 and Table S2).

3.3. Microscopy characterization

Because of the rigorous chemical treatment endured by the material, questioning the integrity of the CNOs is one of the main concerns of this study. High-resolution transmission electron microscopy was employed for the discovery of CNOs by Ugarte in 1992, obtaining the material formation under electron beam irradiation [2]. The high magnification reached by this permits the direct observation of onions morphology, as well as the presence of nanographene particles and amorphous carbon. Indeed, p-CNO TEM images (Fig. 2A–B) show aggregates with dimensions above 100 nm, and the presence of small particles of low contrast resembling nanographene sheets, probably produced during carbon nanodiamonds annealing (Red arrow in Fig. 2 A, B). No presence of isolated particles was observed in the sample, confirming our conclusion on the strong aggregation. The result obtained for ox-CNOs indicate the opposite. The images of single CNOs are represented in Fig. 2D and E. The concentric layered morphology is clearly visible in the images, confirming the integrity of the material and the effectiveness of the strong acidic treatment. In addition, a peculiar particle is reported in Fig. 2F. This resembles two fused onions, in a concentric lemniscate-like structure (∞), pointing to the presence of covalent bonds between them. These results highlight the relevance of our AUC study in solution to distinguish post-drying non-covalent aggregates from actual covalent ensembles. The observation of this structure, again, corroborates the hypothesis that CNOs produced under Ar or He flow tend to covalently aggregate together and grow also as fused structures. Confirming our AUC measurements, neither in 6 M-CNOs (Fig. 2G–I) nor in NH_4OH–CNOs (Fig. 2J-L), individual CNOs were observed.

In contrast to the bulk spectroscopic techniques typically used in CNT research, we aimed to characterize single CNOs to discern their chemical composition. To tackle this challenge, ox-CNO particles were investigated by STEM-MAADF/HAADF analysis (using an aberration corrected Nion UltraSTEM 100 dedicated scanning transmission electron microscope with an acceleration voltage of 60 kV). This permits analysis with lower irradiation energy than HRTEM (200 eV) avoiding possible particle modification and providing precise elemental analysis at the same time.

STEM-MAADF images show typical CNOs with spherical shape and diameters between 5 and 10 nm (Fig. 3A and B). Moreover, we also observe an individual example of a relatively large polygonal particle (Fig. S2) [20]. Finally, we employed electron energy loss spectroscopy and spectral mapping within the same instrument to analyze the oxygen content of the onions with spatial resolution. We recorded 32 × 32 pixels spectrum maps over several CNOs. Because of a low oxygen content in the single pixel spectra, the signal was summed over the area of 9 × 9 pixels to evaluate the oxygen distribution across the sample (Fig. 3C). The background was subtracted for each pixel before the average spectra was calculated. The oxygen K edge at 532 eV indicates the presence of oxygen across the sample, even though definite distribution cannot be resolved due to varying sample thickness. Nonetheless, localizing the average calculated area at the edges and the center of the particles, the oxygen content resulted lower at the edges and higher at the center, indicating a dependence of oxygen to carbon distribution (Fig. S3), and highlighting the homogeneous distribution across the surface.

The low oxygen content (low intensity) could be explained by the

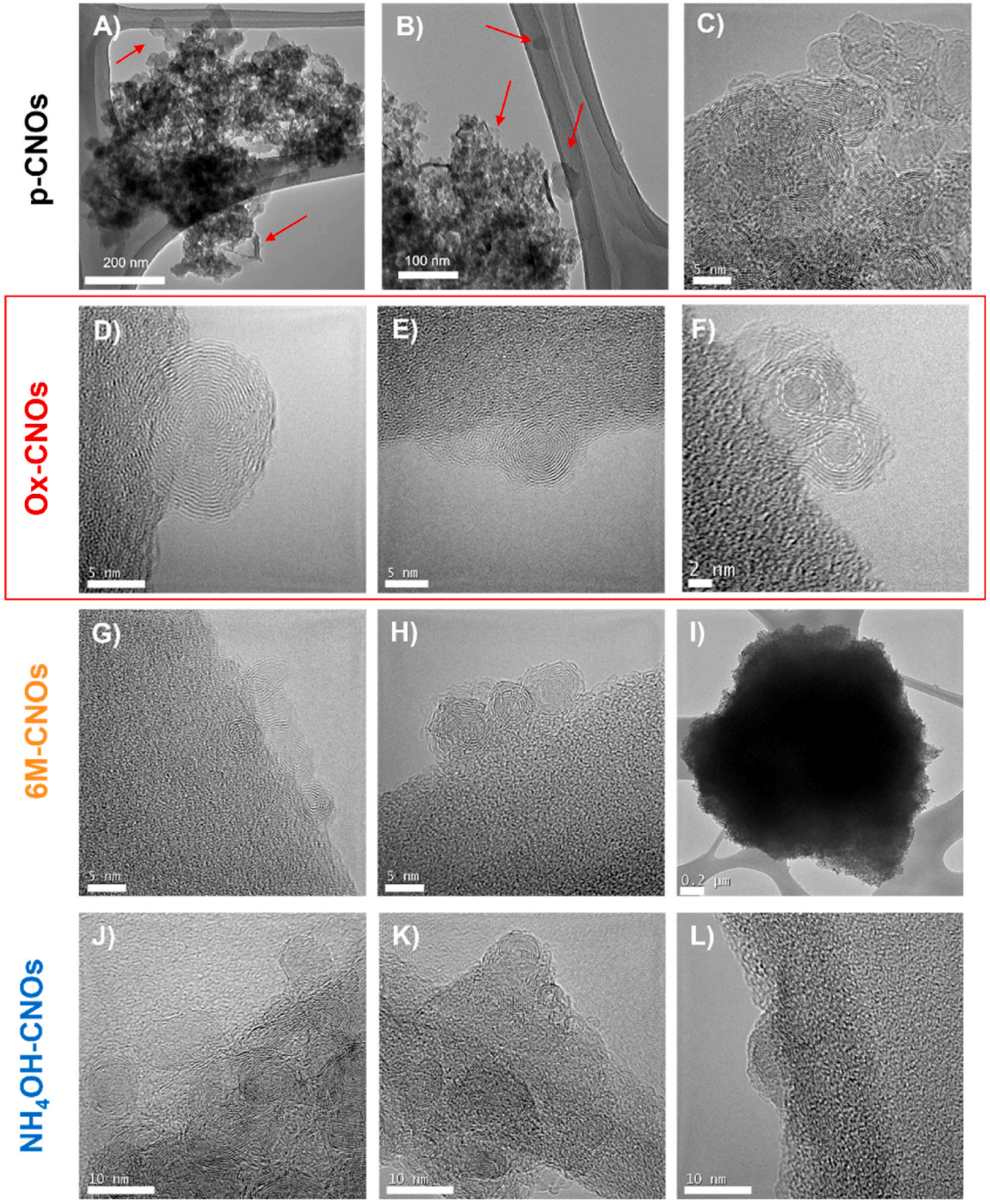

Fig. 2. HRTEM images of different CNOs samples. A-C) p-CNOs after NMP dispersion. The red arrows indicate non-individual particles observed on the sample. Scale bars represent 200, 100 and 5 nm for A, B, and C respectively; D-F) ox-CNOs, the white dotted line highlights the lemniscate structure. Scale bars represent 5, 5 and 2 nm for D, E, and F respectively; G-I) 6 M-CNOs. Scale bars values represent 5, 5 and 200 nm for G, H, and I respectively; L-N) NH_4OH–CNOs. Scale bars represent 10 nm for J, K, and L. (A colour version of this figure can be viewed online.)

pre-treatment to which the sample were subjected before the STEM-MAADF analysis. The grid with the ox-CNOs was indeed heated at 180 °C for at least 8 h under vacuum before entering the microscope column. It is reasonable to assume that part of the oxide groups were annihilated with this treatment, with a consequent decrease in the oxygen content, as also indicated by thermogravimetric analysis, showing low weight loss from 110 °C (Section 3.4 and Fig. S6).

3.4. Raman spectroscopy

Raman spectroscopy is a fundamental tool for carbon nanomaterials characterization, giving direct information about their crystalline structure, defects (intended as sp^3 to sp^2 carbon atom ratio) as well as electronic valence band modifications [49–51]. Raman spectra of carbon nanomaterials is constituted by three main bands, called in order, D, G, and 2D. The so-called D band (1330-1342 cm^{-1} for graphene) is

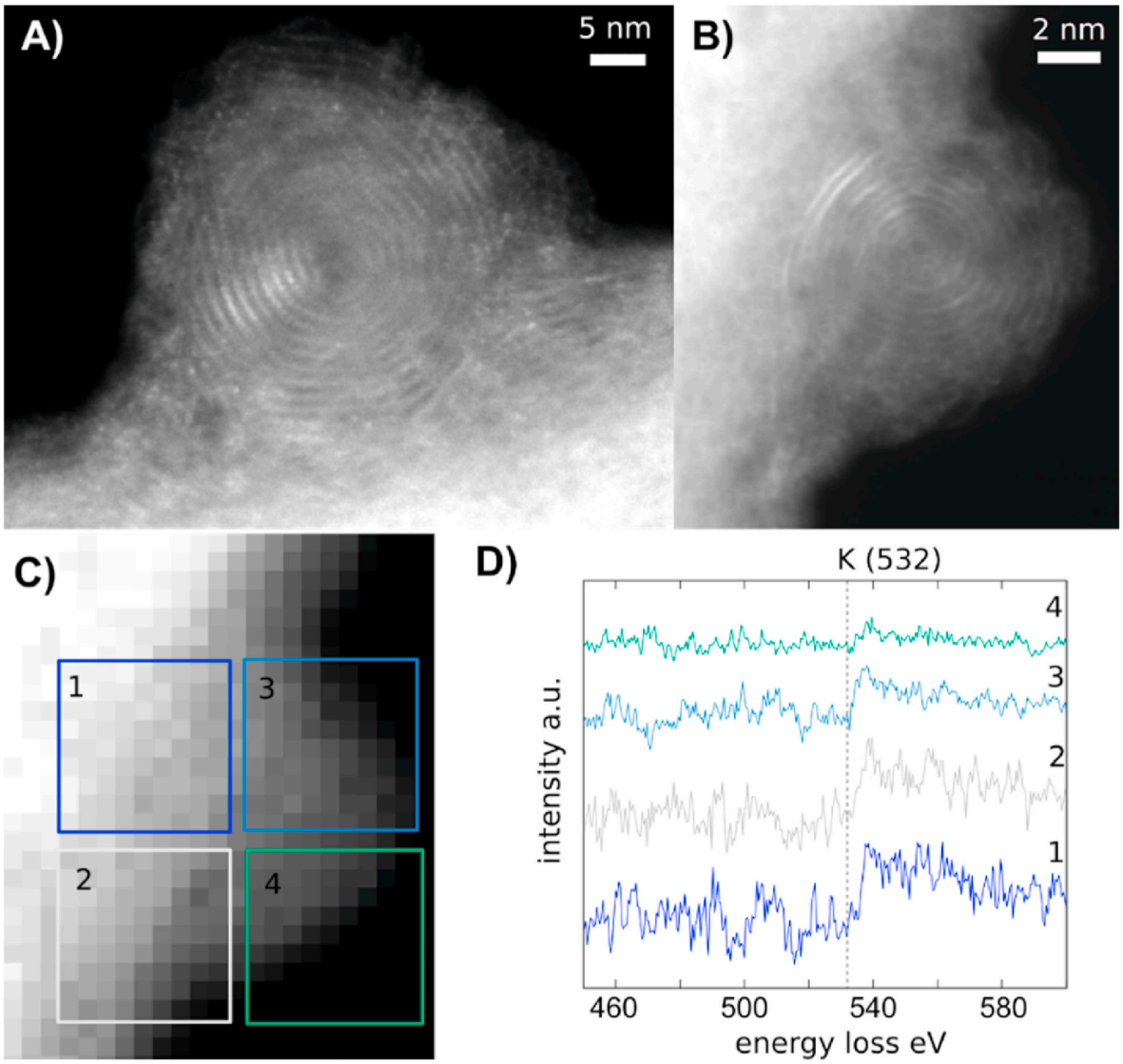

Fig. 3. MAADF-EELs analysis of ox-CNOs. A, B) MAADF CNOs images. The images contain 2048 × 2048 pixels and have been filtered with a Gaussian blur using a radius of 2 and 4 pixels respectively. Scale bars represent 5 and 2 nm for A and B respectively; C) 32 × 32 pixel HAADF spectrum image over the relevant energy range of 530–550 eV of the onion in panel B, analyzed areas are indicated by colored squares; D) Average oxygen signal at the K edge (532 eV) recorded over 9 × 9 pixel areas indicated in panel C. (background is subtracted separately for each pixel). (A colour version of this figure can be viewed online.)

activated in the presence of defects and disorder induced by phonon transitions and is generally related to sp^3 hybridized carbon atoms. The G band, (1580–1590 cm^{-1} for graphene) arises from the first-order peak with E_{2g}-symmetry and is related to sp^2 hybridized carbon atoms. Finally, the 2D band (~2700 cm^{-1}) is activated via double-resonance of phonons at the K-point in the Brillouin zone [49,52]. The peak position also gives information about the material morphology, indeed the G band is expected to be shifted at higher energy values for CNOs compared to graphene due to their surface tension (between 1590 and 1610 cm^{-1}) [17,53]. Moreover, for a correct spectra deconvolution, other contribution must be taken into account. We have therefore fitted the Raman spectra including the contributions of the D*, D″, D′, G* and D + G bands, similarly to what reported by Bogdanov and Zeiger for CNOs [20,21] and by Ferrari, Claramunt and Lee for graphene oxide [54–56]. The D* is commonly attributed to sp^3 orbital, observed in nanocrystalline diamonds, while the D″ band was observed in soot and carbon black samples, but its origin is still controversial. However, the discussion about the physical origins of these band goes beyond the objectives of this study, and we leave their description to more specialized chemical-physical investigations of carbon nanomaterial Raman spectroscopy [49,54,55,57]. Herein, we report the average Raman spectra deduced from statistic Raman mapping, obtained by analysis of more than 400 single point spectra per sample in order to unveil the spectroscopic shifts (Fig. S4 for spectra deconvolution) [4,58,59]. p-CNOs and NH_4OH–CNOs spectra are almost identical, with D and G bands at ~1339 and 1579 cm^{-1} respectively, and the 2D band at ~2670 cm^{-1} (Fig. 4A and B, Table 2 and S4). These values are very similar to what was reported by Zeiger et al. [21] for CNOs produced under Ar atmosphere at 1700 °C and by Bogdanov et al. [20], both presenting nanographite particles, while the G band of the p-CNOs is closer to what was reported for few-layer graphene [20,21]. This behavior could be explained by a contribution given by nanographite particles, shifting the peaks positions to lower energy. Conversely, acid treatment results in an upward shift in the energy of the D and G bands to 1346 and 1588 cm^{-1} for 6M-CNOs, and 1344 and 1588 cm^{-1} for ox-CNOs respectively. The peak positions of these samples suggests a decrease in nanographite particles, with an increased contribution of CNOs to the average spectra. Moreover, from the statistical distribution of peak positions, we can observe that the acid treatment leads to a tightened peak position distribution compared to pristine and

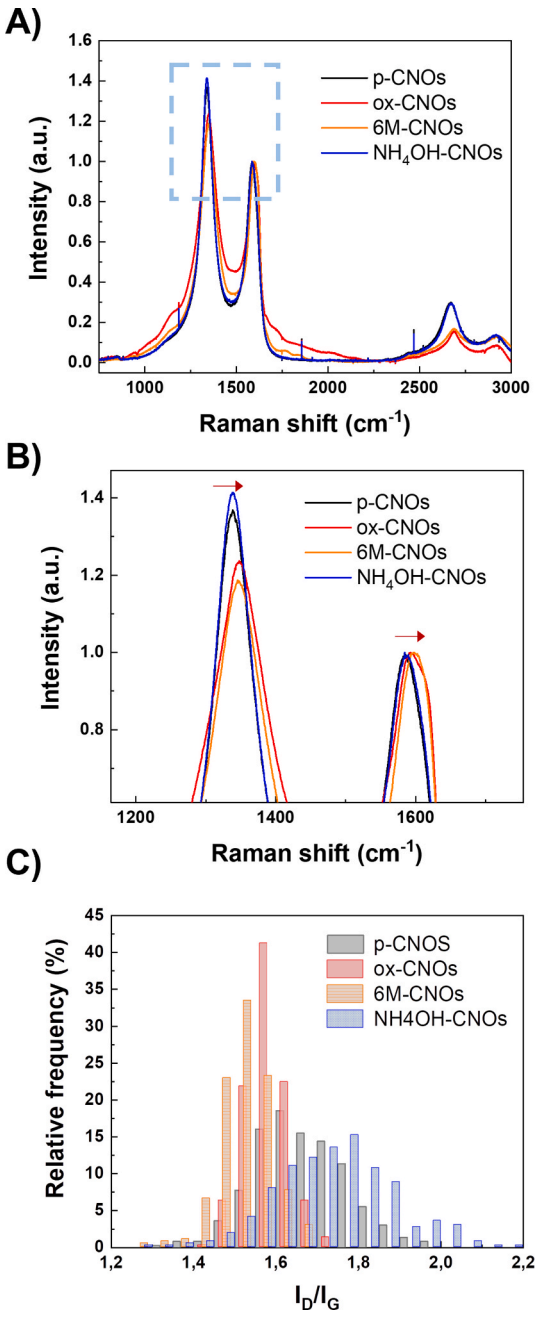

Fig. 4. Raman spectra of CNOs. A) Average Raman spectra obtained from statistical Raman mapping analysis of CNOs (>400 points each spectrum). Spectra are normalized to G intensity for better comprehension. The blue box indicates the section shown in B; B) Magnification of the Raman's spectra D and G band section; C) I_D/I_G ratio distribution from statistical Raman mappings. Red arrows highlight D and G band shifts. (A colour version of this figure can be viewed online.)

base-treated CNOs (Fig. S5). Surprisingly, the I_D/I_G ratio decreased after acid treatments from 1.66 of p-CNOs to 1.58 and 1.53 respectively, accompanied by a significant tightening of the statistical distribution compared to both p-CNOs and NH_4OH–CNOs (Fig. 4C and Figure S6 B-D). One would have expected an increase of this value following the surface oxidation and increase of outer defects. However, it is possible to explain this behavior based on the Ferrari and Robertson model on the correlation between I_D/I_G ratio and graphene defects. The models propose two different behaviors of the I_D/I_G relation with increased defects rates, one characterized by linearly increasing values when defects are located at a distance above 2 nm, followed by a non-linear decrease when defects distance is below 2 nm. Taking into account that the acid treatment reduces onion aggregation (until single onions in the case of ox-CNOs), yielding particles with diameters <10 nm, and that the CNOs' surface is oxidized (*vide infra* for XPS analysis), we can assume that this treatment increases the surface defects to a distance below 2 nm, falling in the non-linear I_D/I_G ratio behavior region [17,50]. These conjectures are supported by the evaluation of the area ratio (A_D/A_G), and by the intensity ratio of D* and D" (I_{D*}/I_G and $I_{G"}/I_G$). In the first case, the A_D/A_G increases its value after an increased treatment strength (Table 2), suggesting an augmentation of CNOs surface's defects. Nonetheless, the common discussion of CNOs Raman analysis only present I_D/I_G values, making a comparison difficult based on this value. In the second case, both values increase (I_{D*}/I_G from 0.08 to 0.11 and 0.19, $I_{G"}/I_G$ from 0.18 to 0.24 and 0.38 respectively; Table S5) indicating an increase of sp^3 carbon atoms, probably due to the formation of oxide groups on the surface.

Finally, it is remarkable that the Raman signal intensity increases with the increase of acid concentration. While NH_4OH–CNOs showed little intensity increase, 6M-CNOs and ox-CNOs showed an intensity increase of 2.5 and 4.5-fold respectively compared to p-CNOs, suggesting more isolated particles and lower signal attenuation (Fig. S6A).

3.5. XPS and TGA characterizations

The surface chemical composition after the chemical treatments was analyzed by XPS. As expected, ox-CNOs are the most oxidized species, followed by 6M-CNOs and NH_4OH–CNOs, with an oxygen content of ~19, 12.4 and 4.2 %, respectively (Table 3), similar to what was reported by Datsyuk et al. for CNTs [42]. By deconvolution of the high-resolution carbon spectra, we estimated the contribution of different functional groups to the oxygen content, similar to what was reported for graphene and graphene oxide. This appears to be mostly due to carboxylic (531.5 eV) and hydroxylic groups (533.5 eV) in the case of acid treatments, while the small amount of oxygen content arising after piranha treatment appears to be constituted mostly by ketones and hydroxyl groups (Fig. S7).

From the analysis of the Auger C KLL derivative spectrum, we calculated the D parameter, related to the sp^2/sp^3 carbon atoms ratio, largely employed for the analysis of different carbon materials, such as graphene, CNTs, and ND [60–63]. This parameter is reported to be 22.5 for graphite (100% sp^2) and 14.5 for diamonds (100% sp^3). It's possible to evaluate the sp^2/sp^3 ratio from its linear interpolation [62,64]. In this study, the D parameter for pristine CNOs was calculated to be 22, corresponding to a sp^2/sp^3 percent distribution of 94/6. NH_4OH–CNOs were less affected by the treatment, with a D value of 21.5. As one could expect, at the increase of the acid concentration we observed a decrease of the D parameter, to 21 and 20 for 6 M – and ox-CNOs respectively. These results are in agreement with what is reported for multi-walled CNTs (MWCNTs) [62], that can be seen as the structurally closest carbon material to CNOs.

Thermogravimetric analysis (TGA) indicates p-CNOs high thermal stability, with no weight loss until the temperature of 1000 °C (Fig. S8). The other three samples showed similar weight loss profiles, NH_4OH–CNOs having the smallest loss, while 6 M – and ox-CNOs present a very similar behavior, with a slow gradual thermal decomposition

Table 2
Raman peak position of CNO samples.

Sample	I_D/I_G	I_{2D}/I_G	A_D/A_G	A_{2D}/A_G	D band	G band	2D band
p-CNOs	1.66	0.35	2.59	0.79	1339	1578	2667
6 M-CNOs	1.58	0.19	3.25	0.46	1346	1589	2686
ox-CNOs	1.53	0.19	3.31	0.58	1347	1588	2685
NH_4OH–CNOs	1.74	0.36	2.66	0.76	1339	1580	2671

Table 3
Percentual atomic surface composition of CNOs after different treatments from XPS analysis. The percentage of the functional group is calculated over the total content of oxygen in the samples.

Atoms	Pristine	ox-CNOs	6M-CNOs	NH_4OH–CNOs
C%	99.08	79.25	86.91	94.92
O%	0.91	18.97	12.42	4.24
N%	–	1.28	0.67	0.66
D parameter	22	20	21	21.5
sp^2/sp^3 (%)	94/6	69/31	81/19	88/12
COOH (531.5 eV)%	27.75	47.3	36.6	8.8
C═O (532.3)%	40.8	–	–	44.2
C–OH (533.5)%	–	40.7	38.1	38.1

occurring from 200 °C and a total weight loss at 600 °C of ~10%, similar to previous reports for graphene oxide [65].

3.6. DLS analysis

Furthermore, we focused our efforts on finding a more widespread and easier-to-use bench alternative to AUC for CNO dispersion analysis. DLS is a common technique employed to evaluate hydrodynamic diameters of nanoparticles in daily routine laboratory work. Its outcome depends on several factors, reaching from sample light absorption, concentration, and stability in solution. Big aggregates, even if scarcely present, can affect the final analysis, and lead to an overestimation of the particle size due to their major contribution in the scatter process. Besides, the particles' surface charge can be evaluated using ζ-potential analysis, obtaining valuable information about the particles' colloidal stability. We have therefore conducted ζ-potential measurements of ox-CNO dispersions at different pH values using an automatic titration system, to understand the effect of functional groups protonation on the CNOs stability. Furthermore, to partially mimic the AUC technique, the final CNO dispersions (p-CNOs in NMP, ox-CNOs in H_2O) were analyzed before and after centrifugation (0.05 mg/mL, 20000 RCF, 30 min) to remove the influence of residual aggregates (above 50 nm), developing a simple method to evaluate the CNOs' hydrodynamic size distribution. ox-CNOs ζ-potential absolute value exhibited an increasing trend at the increment of pH (−25, −32, and −35 mV at pH 3, 7, and 14 respectively). It is worth mentioning that samples at pH < 3 aggregated at a fast ratio that hindered the measurements. This behavior was to be expected since ox-CNOs contain oxidized surface groups. Indeed, carboxylic acid deprotonation at higher pH values leads to the increase of negative charge, decreasing aggregation and ameliorating particle colloidal stability. The hydrodynamic diameter evaluated during the repetitive measurement showed a homogeneous and stable value above pH 5 between 50 and 70 nm (Fig. S9). However, as anticipated, this value is affected by the presence of CNO aggregates. By subjecting the dispersions to short centrifugation times, the biggest aggregates sedimented, revealing a distribution with smaller sizes (Fig. 5). At pH 7 the

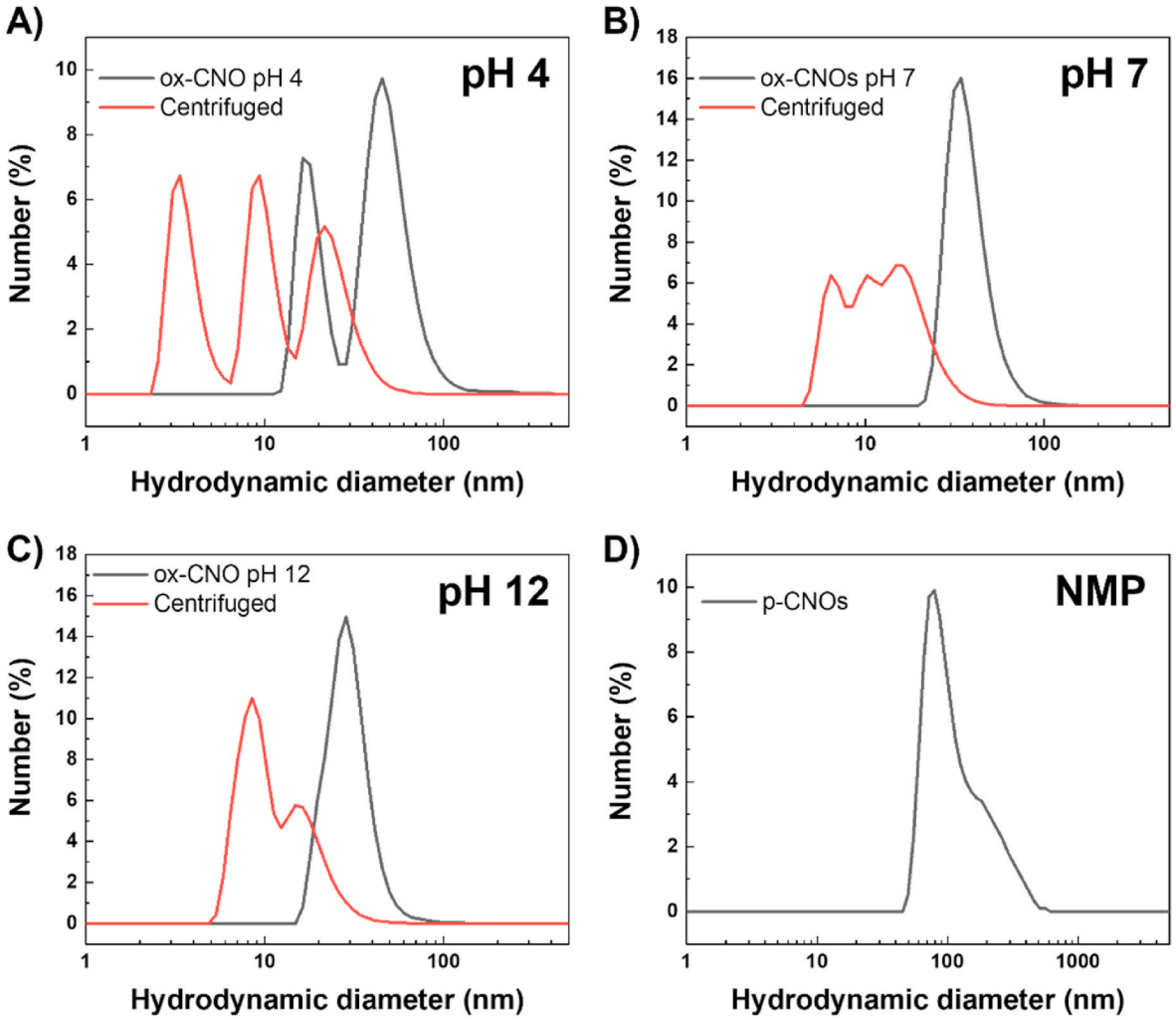

Fig. 5. p-CNOs and ox-CNOs DLS hydrodynamic diameter evaluated before and after centrifugation (black and red line respectively) at different pH. A) ox-CNOs at pH 4; b) ox-CNOs at pH 7; C) ox-CNOs at pH 12; D) p-CNOs in NMP before centrifugation. (A colour version of this figure can be viewed online.)

particles' aggregation decreased from ~34 nm (30–100 nm distribution) to a distribution between 5 and 40 nm, with three main peaks of ~7, 10, and 16 nm, in complete agreement with AUC measurements conducted for the same media. Similar behavior was observed at pH 12, with two main peaks after centrifugation at ~9 and 28 nm. In general, non-centrifuged dispersions slightly decreases their hydrodynamic diameter at the increase of pH (from 46, 34, and 26 nm respectively), as a consequence of deprotonation and the increase of surface charges. Partially different is the case of the pH 4 dispersion. The non-centrifuged sample presented two populations (16 and 46 nm) and a triple separation of the dispersion after centrifugation, at ~ 4, 9, and 21 nm. On the other hand, pristine CNOs in NMP showed a wider distribution (44–540 nm) with a main population at ~ 79 nm before centrifugation, while sedimented completely after centrifugation. With this last analysis, we have demonstrated that pre-centrifugation can be employed as a tool to remove big aggregates (even if in small amounts) which mask the real size distribution, allowing the straightforward use of DLS to determine the CNOs lateral size distribution.

It is worth mentioning here that by means of these results, it is possible to rationally separate CNOs by centrifugation, obtaining rich dispersions of individual onions. ox_3-CNOs in H_2O (pH ~ 5.5 after first step of cleaning, conc. ~ 3 mg/mL) was centrifuged at 18500 RCF for 30 min and the supernatant recovered from the sediment. Indeed, AUC analysis revealed a D_{50} value of 12 nm mostly, with a main population of ~7 nm, therefore mostly constituted by individual CNOs (Fig. S10, Table S6). On the other hand, the sediment distribution presented a D_{50} value of ~83 nm, confirming the possibility of obtaining dispersions with great separation between individual CNOs and aggregates.

3.7. Electronic properties

Finally, we investigated the electronic properties of treated CNOs in comparison to p-CNOs. For this, small pellets were obtained by pressing 5 mg of dry powder at 3 atm. The impedance of the samples was measured by a two-point system. p-CNOs were the most resistive material, with a value of ~12 Ω/cm (Fig. 6). Interestingly, contrary to expectation, individualized ox-CNOs presented higher conductivity, with a resistance of only ~3 Ω/cm, showing great potential for electrochemical applications. Following a similar trend to the other characterization techniques, 6M-CNOs exhibited a value of ~3.7 Ω/cm and NH_4OH–CNOs a value of ~7 Ω/cm. This result illustrates the importance of the CNOs separation, suggesting that the single particles can be processed in pellets with better conductivity than pristine CNOs attributed to their improved packing, despite their higher surface oxidation.

4. Conclusion

In this work, we have systematically investigated different methodologies for carbon nano-onions separation. CNO aggregation is observed during their conversion by thermal annealing of carbon nano diamonds, hindering scientists from working with individual fullerene-like carbon nanomaterials. Applying physical and chemical techniques we demonstrated that only the application of strong oxidizing acid treatment allow for CNO individualization, increasing their water dispersibility, while other treatments (e.g. prolonged sonication, mild acid conditions) are not sufficient to achieve a complete separation. In addition, we propose analytical ultracentrifugation as the gold standard technique for a complete ensemble characterization of CNOs directly in dispersion, overcoming re-aggregation issues upon sample preparation typical of microscopy techniques, and we suggest a methodology to correlate these dispersions by DLS analysis. The results obtained from this study indirectly indicate that CNOs aggregation is likely a result of covalent interactions among the particles formed during production, rather than being hindered by graphitic layers that prevent their dispersion. We believe that the accomplishments showcased here will provide a significant contribution and will help to enhance the research centered around CNOs, especially in fields such as nanomedicine, electrochemistry, and energy storage.

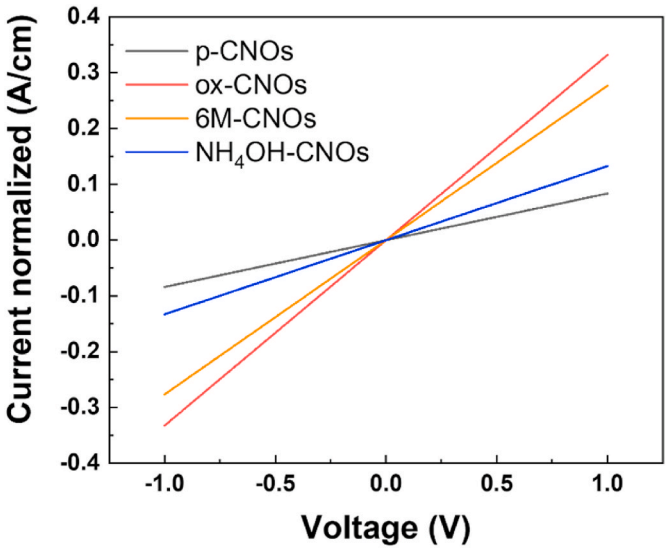

Fig. 6. Normalized current (A/cm) vs voltage graph of CNOs samples. Data showed represent the fitting of the I/V curve. The current was normalized to area/length (cm^2/cm) of the sample for a correct comparison. (A colour version of this figure can be viewed online.)

CRediT authorship contribution statement

Matteo Andrea Lucherelli: Conceptualization, Data curation, Formal analysis, Investigation, Methodology, Writing – original draft. **Lisa M.S. Stiegler:** Data curation, Formal analysis, Investigation, Methodology, Validation, Writing – original draft. **Florian Steiger:** Data curation, Formal analysis, Investigation, Methodology, Visualization. **E. Harriet Åhlgren:** Data curation, Formal analysis, Investigation, Methodology, Visualization, Writing – original draft. **Julia Requena-Ramírez:** Data curation, Investigation, Methodology. **Edison Castro:** Investigation, Methodology, Validation, Writing – review & editing. **Luis Echegoyen:** Methodology, Project administration, Resources, Supervision, Validation. **Andreas Hirsch:** Funding acquisition, Methodology, Project administration, Resources, Supervision. **Wolfgang Peukert:** Funding acquisition, Methodology, Project administration, Resources, Supervision, Validation. **Jani Kotakoski:** Data curation, Formal analysis, Funding acquisition, Investigation, Methodology, Resources, Supervision, Validation, Writing – review & editing. **Johannes Walter:** Conceptualization, Data curation, Formal analysis, Investigation, Methodology, Resources, Supervision, Validation, Visualization, Writing – original draft. **M. Eugenia Pérez-Ojeda:** Conceptualization, Data curation, Formal analysis, Funding acquisition, Investigation, Methodology, Project administration, Resources, Validation, Visualization, Writing – review & editing. **Gonzalo Abellán:** Conceptualization, Formal analysis, Funding acquisition, Methodology, Project administration, Resources, Supervision, Validation, Writing – review & editing.

Declaration of competing interest

The authors declare that they have no known competing financial interests or personal relationships that could have appeared to influence the work reported in this paper.

Acknowledgments

This work has been supported by the European Union (ERC-2018-StG 804110-2D-PnictoChem & ERC-Proof of Concept Grant 101101079-

2D4H2), the Spanish MICINN (PID2022-143297NB-I00, PDC2022-133997-I00, TED2021-131347B–I00 and Excellence Unit María de Maeztu CEX2019-000919-M), the Generalitat Valenciana (CIDEGENT/2018/001), the Universitat de València and HUP/IIS La Fe (VLC-BIO-MED AP2022-27). Furthermore, the authors would like to thank the Deutsche Forschungsgemeinschaft (DFG, German Research Foundation) for financial support in scope of Collaborative Research Centre SFB 953 "Synthetic Carbon Allotropes" (Project-ID 182849149, project A03 and A09).

M. A. L. acknowledges the Generalitat Valenciana for a postdoctoral fellowship (CIAPOS/2021/255). EHÅ acknowledges the funding from the Research Council of Finland project number 355011 and JK acknowledge the funding from the Austrian Science Fund (FWF) through the project P34797–N36. The authors thank Dr M. D. Jordán Martín for her kind assistance with the XPS measurements, Ángel López for the impedance measurements, and Christian Olivares for his valuable help in the laboratory.

Appendix A. Supplementary data

Supplementary data to this article can be found online at https://doi.org/10.1016/j.carbon.2023.118760.

References

[1] I. Suarez-Martinez, N. Grobert, C.P. Ewels, Nomenclature of sp carbon nanoforms, Carbon 50 (2012) 741–747, https://doi.org/10.1016/j.carbon.2011.11.002.
[2] D. Ugarte, Curling and closure of graphitic networks under electron-beam irradiation, Nature 359 (1992) 707–709, https://doi.org/10.1038/359707a0.
[3] M.E. Plonska-Brzezinska, Carbon nano-onions: a review of recent progress in synthesis and applications, ChemNanoMat 5 (2019) 568–580, https://doi.org/10.1002/cnma.201800583.
[4] M.E. Pérez-Ojeda, E. Castro, C. Kröckel, M.A. Lucherelli, U. Ludacka, J. Kotakoski, K. Werbach, H. Peterlik, M. Melle-Franco, J.C. Chacón-Torres, F. Hauke, L. Echegoyen, A. Hirsch, G. Abellán, Carbon nano-onions: potassium intercalation and reductive covalent functionalization, J. Am. Chem. Soc. 143 (2021) 18997–19007, https://doi.org/10.1021/jacs.1c07604.
[5] R. Borgohain, J. Li, J.P. Selegue, Y.-T. Cheng, Electrochemical study of functionalized carbon nano-onions for high-performance supercapacitor electrodes, J. Phys. Chem. C 116 (2012) 15068–15075, https://doi.org/10.1021/jp301642s.
[6] K.W. Street, M. Marchetti, R.L. VanderWal, A.J. Tomasek, Evaluation of the Tribological Behavior of Krytox 143AB with Nano-Onions, NASA/TM, 2003. https://ntrs.nasa.gov/citations/20030055622. (Accessed 20 September 2021).
[7] D. Pech, M. Brunet, H. Durou, P. Huang, V. Mochalin, Y. Gogotsi, P.-L. Taberna, P. Simon, Ultrahigh-power micrometre-sized supercapacitors based on onion-like carbon, Nat. Nanotechnol. 5 (2010) 651–654, https://doi.org/10.1038/nnano.2010.162.
[8] M.E. Plonska-Brzezinska, L. Echegoyen, Carbon nano-onions for supercapacitor electrodes: recent developments and applications, J. Mater. Chem. A 1 (2013) 13703–13714, https://doi.org/10.1039/C3TA12628E.
[9] M. Zeiger, N. Jäckel, V.N. Mochalin, V. Presser, Review: carbon onions for electrochemical energy storage, J. Mater. Chem. A 4 (2016) 3172–3196, https://doi.org/10.1039/C5TA08295A.
[10] A. Camisasca, S. Giordani, Carbon nano-onions in biomedical applications: promising theranostic agents, Inorg. Chim. Acta. 468 (2017) 67–76, https://doi.org/10.1016/j.ica.2017.06.009.
[11] I. Alexandrou, H. Wang, N. Sano, G.A.J. Amaratunga, Structure of carbon onions and nanotubes formed by arc in liquids, J. Chem. Phys. 120 (2004) 1055–1058, https://doi.org/10.1063/1.1629274.
[12] H. Lange, M. Sioda, A. Huczko, Y.Q. Zhu, H.W. Kroto, D.R.M. Walton, Nanocarbon production by arc discharge in water, Carbon 41 (2003) 1617–1623, https://doi.org/10.1016/S0008-6223(03)00111-8.
[13] W. Wu, Z. Zhu, Z. Liu, Y. Xie, J. Zhang, T. Hu, Preparation of carbon-encapsulated iron carbide nanoparticles by an explosion method, Carbon 41 (2003) 317–321, https://doi.org/10.1016/S0008-6223(02)00292-0.
[14] J.Y. Huang, H. Yasuda, H. Mori, Highly curved carbon nanostructures produced by ball-milling, Chem. Phys. Lett. 303 (1999) 130–134, https://doi.org/10.1016/S0009-2614(99)00131-1.
[15] V.L. Kuznetsov, A.L. Chuvilin, Y.V. Butenko, I.Yu Mal'kov, V.M. Titov, Onion-like carbon from ultra-disperse diamond, Chem. Phys. Lett. 222 (1994) 343–348, https://doi.org/10.1016/0009-2614(94)87072-1.
[16] A. Palkar, F. Melin, C.M. Cardona, B. Elliott, A.K. Naskar, D.D. Edie, A. Kumbhar, L. Echegoyen, Reactivity differences between carbon nano onions (CNOs) prepared by different methods, Chem. Asian J. 2 (2007) 625–633, https://doi.org/10.1002/asia.200600426.
[17] M. Zeiger, N. Jäckel, M. Aslan, D. Weingarth, V. Presser, Understanding structure and porosity of nanodiamond-derived carbon onions, Carbon 84 (2015) 584–598, https://doi.org/10.1016/j.carbon.2014.12.050.
[18] J. Chen, S.Z. Deng, J. Chen, Z.X. Yu, N.S. Xu, Graphitization of nanodiamond powder annealed in argon ambient, Appl. Phys. Lett. 74 (1999) 3651–3653, https://doi.org/10.1063/1.123211.
[19] S. Tomita, A. Burian, J.C. Dore, D. LeBolloch, M. Fujii, S. Hayashi, Diamond nanoparticles to carbon onions transformation: X-ray diffraction studies, Carbon 40 (2002) 1469–1474, https://doi.org/10.1016/S0008-6223(01)00311-6.
[20] K. Bogdanov, A. Fedorov, V. Osipov, T. Enoki, K. Takai, T. Hayashi, V. Ermakov, S. Moshkalev, A. Baranov, Annealing-induced structural changes of carbon onions: high-resolution transmission electron microscopy and Raman studies, Carbon 73 (2014) 78–86, https://doi.org/10.1016/j.carbon.2014.02.041.
[21] M. Zeiger, N. Jäckel, D. Weingarth, V. Presser, Vacuum or flowing argon: what is the best synthesis atmosphere for nanodiamond-derived carbon onions for supercapacitor electrodes? Carbon 94 (2015) 507–517, https://doi.org/10.1016/j.carbon.2015.07.028.
[22] A. Krüger, F. Kataoka, M. Ozawa, T. Fujino, Y. Suzuki, A.E. Aleksenskii, A.Ya Vul', E. Ōsawa, Unusually tight aggregation in detonation nanodiamond: identification and disintegration, Carbon 43 (2005) 1722–1730, https://doi.org/10.1016/j.carbon.2005.02.020.
[23] J.C. Zuaznabar-Gardona, A. Fragoso, Determination of the Hansen solubility parameters of carbon nano-onions and prediction of their dispersibility in organic solvents, J. Mol. Liq. 294 (2019), 111646, https://doi.org/10.1016/j.molliq.2019.111646.
[24] A. Guo, K. Bao, S. Sang, X. Zhang, B. Shao, C. Zhang, Y. Wang, F. Cui, X. Yang, Soft-chemistry synthesis, solubility and interlayer spacing of carbon nano-onions, RSC Adv. 11 (2021) 6850–6858, https://doi.org/10.1039/D0RA09410B.
[25] C. Backes, T.M. Higgins, A. Kelly, C. Boland, A. Harvey, D. Hanlon, J.N. Coleman, Guidelines for exfoliation, characterization and processing of layered materials produced by liquid exfoliation, Chem. Mater. 29 (2017) 243–255, https://doi.org/10.1021/acs.chemmater.6b03335.
[26] C. Backes, Production of graphene and other two-dimensional nanosheets by liquid phase exfoliation, in: Graphene, Elsevier, 2021, pp. 251–314, https://doi.org/10.1016/B978-0-08-102848-3.00001-3.
[27] M. d' Amora, M. Rodio, J. Bartelmess, G. Sancataldo, R. Brescia, F. Cella Zanacchi, A. Diaspro, S. Giordani, Biocompatibility and biodistribution of functionalized carbon nano-onions (f-CNOs) in a vertebrate model, Sci. Rep. 6 (2016), 33923, https://doi.org/10.1038/srep33923.
[28] M. d'Amora, A. Camisasca, A. Boarino, S. Arpicco, S. Giordani, Supramolecular functionalization of carbon nano-onions with hyaluronic acid-phospholipid conjugates for selective targeting of cancer cells, Colloids Surf. B Biointerfaces 188 (2020), 110779, https://doi.org/10.1016/j.colsurfb.2020.110779.
[29] L. Reinert, M. Zeiger, S. Suárez, V. Presser, F. Mücklich, Dispersion analysis of carbon nanotubes, carbon onions, and nanodiamonds for their application as reinforcement phase in nickel metal matrix composites, RSC Adv. 5 (2015) 95149–95159, https://doi.org/10.1039/C5RA14310A.
[30] J. Bartelmess, E.D. Luca, A. Signorelli, M. Baldrighi, M. Becce, R. Brescia, V. Nardone, E. Parisini, L. Echegoyen, P.P. Pompa, S. Giordani, Boron dipyrromethene (BODIPY) functionalized carbon nano-onions for high resolution cellular imaging, Nanoscale 6 (2014) 13761–13769, https://doi.org/10.1039/C4NR04533E.
[31] M. Frasconi, R. Marotta, L. Markey, K. Flavin, V. Spampinato, G. Ceccone, L. Echegoyen, E.M. Scanlan, S. Giordani, Multi-functionalized carbon nano-onions as imaging probes for cancer cells, Chem. Eur J. 21 (2015) 19071–19080, https://doi.org/10.1002/chem.201503166.
[32] M. Ghosh, S.K. Sonkar, M. Saxena, S. Sarkar, Carbon nano-onions for imaging the life cycle of Drosophila melanogaster, Small 7 (2011) 3170–3177, https://doi.org/10.1002/smll.201101158.
[33] S. Giordani, J. Bartelmess, M. Frasconi, I. Biondi, S. Cheung, M. Grossi, D. Wu, L. Echegoyen, D.F. O'Shea, NIR fluorescence labelled carbon nano-onions: synthesis, analysis and cellular imaging, J. Mater. Chem. B 2 (2014) 7459–7463, https://doi.org/10.1039/C4TB01087F.
[34] Y. Huang, S. Zhang, Y. Chen, H. Dai, Y. Lin, Modular and noncontact wireless detection platform for ovarian cancer markers: electrochemiluminescent and photoacoustic dual-signal output based on multiresponse carbon nano-onions, Anal. Chem. 94 (2022) 13269–13277, https://doi.org/10.1021/acs.analchem.2c03337.
[35] S. K, A. Camisasca, M. Bartkowski, A. Garhwal, P. K, A. Aravind, S. Giordani, DrR. Kurapati, Biodegradability of carbon nano-onions by human myeloperoxidase and the photo-fenton reaction, Chemistry (2023), https://doi.org/10.26434/chemrxiv-2023-jqmbg.
[36] YuV. Butenko, S. Krishnamurthy, A.K. Chakraborty, V.L. Kuznetsov, V.R. Dhanak, M.R.C. Hunt, L. Šiller, Photoemission study of onionlike carbons produced by annealing nanodiamonds, Phys. Rev. B 71 (2005), 075420, https://doi.org/10.1103/PhysRevB.71.075420.
[37] S.N. Bokova-Sirosh, A.V. Pershina, V.L. Kuznetsov, A.V. Ishchenko, S.I. Moseenkov, A.S. Orekhov, E.D. Obraztsova, Raman spectra for characterization of onion-like carbon, J. Nanoelectron. Optoelectron. 8 (2013) 106–109, https://doi.org/10.1166/jno.2013.1444.
[38] E. Meirzadeh, A.M. Evans, M. Rezaee, M. Milich, C.J. Dionne, T.P. Darlington, S. T. Bao, A.K. Bartholomew, T. Handa, D.J. Rizzo, R.A. Wiscons, M. Reza, A. Zangiabadi, N. Fardian-Melamed, A.C. Crowther, P.J. Schuck, D.N. Basov, X. Zhu, A. Giri, P.E. Hopkins, P. Kim, M.L. Steigerwald, J. Yang, C. Nuckolls, X. Roy, A few-layer covalent network of fullerenes, Nature 613 (2023) 71–76, https://doi.org/10.1038/s41586-022-05401-w.

[39] J. Walter, K. Löhr, E. Karabudak, W. Reis, J. Mikhael, W. Peukert, W. Wohlleben, H. Cölfen, Multidimensional analysis of nanoparticles with highly disperse properties using multiwavelength analytical ultracentrifugation, ACS Nano 8 (2014) 8871–8886, https://doi.org/10.1021/nn503205k.
[40] J. Pearson, J. Walter, W. Peukert, H. Cölfen, Advanced multiwavelength detection in analytical ultracentrifugation, Anal. Chem. 90 (2018) 1280–1291, https://doi.org/10.1021/acs.analchem.7b04056.
[41] L. Bao, O. Martin, T. Wei, M.E. Pérez-Ojeda, F. Hauke, A. Hirsch, A straightforward reductive approach for the deoxygenation, activation and functionalization of ultrashort single-walled carbon nanotubes, Carbon 171 (2021) 768–776, https://doi.org/10.1016/j.carbon.2020.09.078.
[42] V. Datsyuk, M. Kalyva, K. Papagelis, J. Parthenios, D. Tasis, A. Siokou, I. Kallitsis, C. Galiotis, Chemical oxidation of multiwalled carbon nanotubes, Carbon 46 (2008) 833–840, https://doi.org/10.1016/j.carbon.2008.02.012.
[43] D.M. Bobrowska, E. Castro, L. Echegoyen, M.E. Plonska-Brzezinska, Carbon nano-onion and zinc oxide composites as an electron transport layer in inverted organic solar cells, ChemNanoMat 6 (2020) 248–257, https://doi.org/10.1002/cnma.201900561.
[44] J. Walter, T. Thajudeen, S. Süβ, D. Segets, W. Peukert, New possibilities of accurate particle characterisation by applying direct boundary models to analytical centrifugation, Nanoscale 7 (2015) 6574–6587, https://doi.org/10.1039/C5NR00995B.
[45] N.C. Garbett, C.S. Mekmaysy, J.B. Chaires, Sedimentation velocity ultracentrifugation analysis for hydrodynamic characterization of G-quadruplex structures, in: P. Baumann (Ed.), G-quadruplex DNA, Humana Press, Totowa, NJ, 2010, pp. 97–120, https://doi.org/10.1007/978-1-59745-363-9_7.
[46] A. Baer, S.E. Wawra, K. Bielmeier, M.J. Uttinger, D.M. Smith, W. Peukert, J. Walter, A.-S. Smith, The Stokes-Einstein-Sutherland Equation at the Nanoscale Revisited, 2023. http://arxiv.org/abs/2302.07359.
[47] T. Premkumar, R. Mezzenga, K.E. Geckeler, Carbon nanotubes in the liquid phase: addressing the issue of dispersion, Small 8 (2012) 1299–1313, https://doi.org/10.1002/smll.201101786.
[48] C. Backes, D. Campi, B.M. Szydlowska, K. Synnatschke, E. Ojala, F. Rashvand, A. Harvey, A. Griffin, Z. Sofer, N. Marzari, J.N. Coleman, D.D. O'Regan, Equipartition of energy defines the size–thickness relationship in liquid-exfoliated nanosheets, ACS Nano 13 (2019) 7050–7061, https://doi.org/10.1021/acsnano.9b02234.
[49] A.C. Ferrari, D.M. Basko, Raman spectroscopy as a versatile tool for studying the properties of graphene, Nat. Nanotechnol. 8 (2013) 235–246, https://doi.org/10.1038/nnano.2013.46.
[50] L.G. Cançado, A. Jorio, E.H.M. Ferreira, F. Stavale, C.A. Achete, R.B. Capaz, M.V. O. Moutinho, A. Lombardo, T.S. Kulmala, A.C. Ferrari, Quantifying defects in graphene via Raman spectroscopy at different excitation energies, Nano Lett. 11 (2011) 3190–3196, https://doi.org/10.1021/nl201432g.
[51] C. Thomsen, S. Reich, J. Maultzsch, Resonant Raman spectroscopy of nanotubes, Philos. Trans. R. Soc. London, Ser. A: Math. Phys. Eng. Sci. 362 (2004) 2337–2359, https://doi.org/10.1098/rsta.2004.1444.
[52] A. Eckmann, A. Felten, I. Verzhbitskiy, R. Davey, C. Casiraghi, Raman study on defective graphene: effect of the excitation energy, type, and amount of defects, Phys. Rev. B Condens. Matter 88 (2013) 1–11, https://doi.org/10.1103/PhysRevB.88.035426.
[53] D. Roy, M. Chhowalla, H. Wang, N. Sano, I. Alexandrou, T.W. Clyne, G.A. J. Amaratunga, Characterisation of carbon nano-onions using Raman spectroscopy, Chem. Phys. Lett. 373 (2003) 52–56, https://doi.org/10.1016/S0009-2614(03)00523-2.
[54] S. Claramunt, A. Varea, D. López-Díaz, M.M. Velázquez, A. Cornet, A. Cirera, The importance of interbands on the interpretation of the Raman spectrum of graphene oxide, J. Phys. Chem. C 119 (2015) 10123–10129, https://doi.org/10.1021/acs.jpcc.5b01590.
[55] A.Y. Lee, K. Yang, N.D. Anh, C. Park, S.M. Lee, T.G. Lee, M.S. Jeong, Raman study of D* band in graphene oxide and its correlation with reduction, Appl. Surf. Sci. 536 (2021), 147990, https://doi.org/10.1016/j.apsusc.2020.147990.
[56] A.C. Ferrari, J. Robertson, Origin of the 1 1 5 0 − cm − 1 Raman mode in nanocrystalline diamond, Phys. Rev. B 63 (2001), 121405, https://doi.org/10.1103/PhysRevB.63.121405.
[57] A.C. Ferrari, J. Robertson, Raman spectroscopy of amorphous, nanostructured, diamond–like carbon, and nanodiamond, Philos. Trans. R. Soc. London, Ser. A: Math. Phys. Eng. Sci. 362 (2004) 2477–2512, https://doi.org/10.1098/rsta.2004.1452.
[58] F. Hof, S. Bosch, J.M. Englert, F. Hauke, A. Hirsch, Statistical Raman spectroscopy: a method for the characterization of covalently functionalized single-walled carbon nanotubes, Angew. Chem. Int. Ed. 51 (2012) 11727–11730, https://doi.org/10.1002/anie.201204791.
[59] J.M. Englert, P. Vecera, K.C. Knirsch, R.A. Schäfer, F. Hauke, A. Hirsch, Scanning-Raman-microscopy for the statistical analysis of covalently functionalized graphene, ACS Nano 7 (2013) 5472–5482, https://doi.org/10.1021/nn401481h.
[60] Y. Mizokawa, T. Miyasato, S. Nakamura, K.M. Geib, C.W. Wilmsen, The C *K L L* first-derivative x-ray photoelectron spectroscopy spectra as a fingerprint of the carbon state and the characterization of diamondlike carbon films, J. Vac. Sci. Technol. A: Vacuum, Surfaces, and Films 5 (1987) 2809–2813, https://doi.org/10.1116/1.574312.
[61] J.C. Lascovich, R. Giorgi, S. Scaglione, Evaluation of the sp2/sp3 ratio in amorphous carbon structure by XPS and XAES, Appl. Surf. Sci. 47 (1991) 17–21, https://doi.org/10.1016/0169-4332(91)90098-5.
[62] L. Stobinski, B. Lesiak, L. Kövér, J. Tóth, S. Biniak, G. Trykowski, J. Judek, Multiwall carbon nanotubes purification and oxidation by nitric acid studied by the FTIR and electron spectroscopy methods, J. Alloys Compd. 501 (2010) 77–84, https://doi.org/10.1016/j.jallcom.2010.04.032.
[63] S. Kaciulis, A. Mezzi, P. Calvani, D.M. Trucchi, Electron spectroscopy of the main allotropes of carbon: electron spectroscopy of graphene, graphite, and diamond, Surf. Interface Anal. 46 (2014) 966–969, https://doi.org/10.1002/sia.5382.
[64] J.C. Lascovich, S. Scaglione, Comparison among XAES, PELS and XPS techniques for evaluation of Sp2 percentage in a-C:H, Appl. Surf. Sci. 78 (1994) 17–23, https://doi.org/10.1016/0169-4332(94)90026-4.
[65] D.A. Jasim, L. Newman, A.F. Rodrigues, I.A. Vacchi, M.A. Lucherelli, N. Lozano, C. Ménard-Moyon, A. Bianco, K. Kostarelos, The impact of graphene oxide sheet lateral dimensions on their pharmacokinetic and tissue distribution profiles in mice, J. Contr. Release 338 (2021) 330–340, https://doi.org/10.1016/j.jconrel.2021.08.028.